

Ion-neutral Interactions and Nonequilibrium Ionization in the Solar Chromosphere

Juan Martínez-Sykora^{1,2,4,5}, Jorrit Leenaarts³, Bart De Pontieu^{2,4,5}, Daniel Nóbrega-Siverio^{4,5}, Viggo H. Hansteen^{1,2,4,5}, Mats Carlsson^{4,5}, and Mikolaj Szydlarski^{4,5}

Bay Area Environmental Research Institute, Moffett Field, CA 94035, USA; juanms@lmsal.com

Lockheed Martin Solar and Astrophysics Laboratory, Palo Alto, CA 94304, USA

³ Institute for Solar Physics, Department of Astronomy, Stockholm University, AlbaNova University Centre, SE-106 91 Stockholm, Sweden Institute of Theoretical Astrophysics, University of Oslo, P.O. Box 1029 Blindern, N-0315 Oslo, Norway Received 2019 October 11; revised 2019 December 3; accepted 2019 December 13; published 2020 January 29

Abstract

The thermal structure of the chromosphere is regulated through a complex interaction of various heating processes, radiative cooling, and the ionization degree of the plasma. Here, we study the impact on the thermal properties of the chromosphere when including the combined action of nonequilibrium ionization (NEI) of hydrogen and helium and ion–neutral interaction effects. We have performed a 2.5D radiative magnetohydrodynamic simulation using the *Bifrost* code. This model includes ion–neutral interaction effects by solving the generalized Ohm's law (GOL) as well as NEI for hydrogen and helium. The GOL equation includes ambipolar diffusion and the Hall term. We compare this simulation with another simulation that computes the ionization in local thermodynamic equilibrium (LTE) including ion–neutral interaction effects. Our numerical models reveal substantial thermal differences in magneto-acoustic shocks, the wake behind the shocks, spicules, low-lying magnetic loops, and the transition region. In particular, we find that heating through ambipolar diffusion in shock wakes is substantially less efficient, while in the shock fronts themselves it is more efficient, under NEI conditions than when assuming LTE.

Unified Astronomy Thesaurus concepts: Solar chromosphere (1479); Solar chromospheric heating (1987); Magnetohydrodynamical simulations (1966); Solar magnetic fields (1503); Solar spicules (1525); Radiative magnetohydrodynamics (2009)

Supporting material: animations, data behind figures

1. Introduction

Ion-neutral interaction and nonequilibrium ionization (NEI) are key physical processes in the solar chromosphere and transition region (TR). Most studies investigating these processes are focused on either one or the other process, but due to their complex physics and the associated high computational cost of modeling such systems (see the review by Ballester et al. 2018, and references therein), they have not hitherto been studied in combination.

Hydrogen has an ionization/recombination timescale of 10^3 – 10^5 s in the chromosphere (Carlsson & Stein 1992, 2002) (except in shock fronts, where it is shorter). This is a very long time compared to typical magnetohydrodynamic (MHD) timescales, which are on the order of 10–100 s. Likewise, Golding et al. (2014) found that the ionization/recombination timescale of helium is on the order of 10^2 – 10^3 s, also longer than the MHD timescales in the chromosphere and TR. NEI effects for heavier atoms occur on timescales shorter than about 10–100 s for typical density values for the TR and corona (Smith & Hughes 2010).

A major consequence of the long ionization and recombination timescales is that the solar plasma exhibits larger temperature fluctuations than what is predicted based on local thermodynamic equilibrium (LTE) ionization. When gas is suddenly heated, the extra energy is not used to ionize hydrogen or helium, but instead mainly increases the thermal energy—and thus the temperature. When gas is suddenly cooled, e.g., by expansion in the wake of a shock front, little energy is released through recombination and the temperature drops more than in LTE.

The ionization degree of the hydrogen (defined here as $F_{\rm Hion} = n_{\rm H\,II}/(n_{\rm H\,I} + n_{\rm H\,II})$, where $n_{\rm H\,I}$ and $n_{\rm H\,II}$ are density number of, respectively, neutral and ionized hydrogen) in the plasma becomes rather insensitive to temperature in NEI. In earlier 2D simulations of the solar chromosphere, $F_{\rm Hion}$ increased from 10^{-5} to 10^{-4} in the upper photosphere to close to unity in the TR, while the bulk of the chromosphere had $F_{\rm Hion} \approx 10^{-2}$ (Leenaarts et al. 2007a).

NEI also removes bands of "preferred temperatures," corresponding to hydrogen and helium ionization temperatures in simulations that assume LTE (Leenaarts et al. 2011; Golding et al. 2016). Additionally, NEI leads to differences in the emergent intensities of spectral lines, either directly because of nonequilibrium level populations (Golding et al. 2017), or indirectly through the changes in the electron density for spectral lines that otherwise can be modeled using statistical equilibrium (e.g., Wedemeyer-Böhm & Carlsson 2011; Leenaarts et al. 2013).

The chromosphere is partially ionized. The ion-neutral collision frequency is small enough for ion-neutral interaction effects to be relevant for the thermodynamics of the chromosphere (e.g., Vernazza et al. 1981; Khomenko & Collados 2012; Martínez-Sykora et al. 2017a). Some ion-neutral interaction effects in the chromosphere can be taken into account by relaxing the MHD constraints and using the so-called generalized Ohm's law (GOL), which includes, at least, the Hall term and ambipolar diffusion. This simplified approach improves the computational efficiency of simulations when comparing to multi-fluid models, since ion-neutral interaction effects are included in a formulation using only a single fluid. The approximation underlying the use of GOL is valid as long as

the velocity drift between ions and neutrals is small compared to velocities from waves and flows (e.g., Cowling 1957; Braginskii 1965; Parker 2007; Ballester et al. 2018). As shown in Martínez-Sykora et al. (2012), this assumption is fulfilled in most of the chromosphere.

Ion-neutral interaction effects, i.e., the ambipolar diffusion and to some extent the Hall term, play a role in many physical processes. First, ion-neutral interactions can cause significant damping of Alfvén waves, especially for high frequencies (De Pontieu et al. 2001; Zagarashvili et al. 2012; Soler et al. 2015), potentially substantially reducing the energy flux that reaches the corona. Second, magnetic field could slip through the chromospheric material (Leake & Arber 2006; Arber et al. 2007; Leake & Linton 2013; Martínez-Sykora et al. 2016), and magnetic energy can be dissipated and lead to heating due to the presence of the ambipolar diffusion (Goodman 2011; Khomenko & Collados 2012; Martínez-Sykora et al. 2017a). Third, ambipolar diffusion has been shown to be a potential key process in triggering type II spicules, and associated with the formation of these spicules, in driving Alfvénic waves (Martínez-Sykora et al. 2017b).

The simulations of Martínez-Sykora et al. (2012, 2015, 2017a) show variations of many orders of magnitude in the ionization degree—and consequently, in the ion-neutral collision frequency within the same scale height. This is a consequence of the assumption that the ionization follows Saha–Boltzmann statistics (LTE), which predicts ionization degrees for hydrogen ranging from ~10⁻¹⁰ for cold areas up to ~1 for shocks and other hot areas in the chromosphere. Since the ambipolar diffusion scales roughly as the inverse of the ionization degree, this produces similar large variations. NEI leads to ionization degrees that are rather constant for a given plasma parcel. We thus expect large changes in the magnitude of ambipolar diffusion effects when using NEI instead of utilizing LTE ionization. The aim of this paper is to investigate the thermal properties of the chromosphere when NEI and ionneutral effects are included at the same time.

The layout of this manuscript is as follows. We briefly describe the Bifrost code (Gudiksen et al. 2011), numerical methods, the setup of the simulations, and their physical processes in Section 2. We study the impact of ion–neutral interaction effects and NEI by comparing and analyzing the following two simulations: (a) one that takes into account ion-neutral interactions while also assuming LTE; and (b) another that computes the ion-neutral interaction effects and the NEI of hydrogen and helium. We analyze these models in detail in Section 3, where we concentrate our discussion on the following topics: general aspects of the thermodynamic, ambipolar diffusion, and NEI properties (Section 3.1); the impact of the NEI on the ambipolar diffusion (Section 3.2), and their impact on the chromospheric thermodynamics (Section 3.3), with special focus on the cold wake behind chromospheric magneto-acoustic shocks and cold regions within type II spicules (Section 3.3.1), the shocks as well as the hot regions within type II spicules (Section 3.3.2), and lowlying chromospheric and TR loops (Section 3.3.3). We end with a discussion and conclusions in Section 4.

2. Numerical Model

We have performed two 2.5D radiative MHD simulations using the *Bifrost* code. The simulations differ in their treatment

of the ionization balance. These two simulations include a common set of physics packages: radiative transfer with scattering in the photosphere and lower chromosphere (Skartlien 2000; Hayek et al. 2010), upper chromospheric and TR radiative losses and gains following Carlsson & Leenaarts (2012) recipes, optically thin radiative losses in the corona, thermal conduction along the magnetic field (Gudiksen et al. 2011), and ion–neutral effects using the GOL (Martínez-Sykora et al. 2017a; D. Nóbrega-Siverio et al. 2019, in preparation). In addition, an ad hoc heating term is included to ensure that the temperature does not drop far below the validity range of our equation of state (~1800 K).

Both simulations have the same spatial resolution, domain size, and magnetic field configuration. The numerical domain spans 90 Mm horizontally and goes from 3 Mm below to 40 Mm above the photosphere (see Figure 1, which is trimmed in order to reveal the structures of the lower atmosphere). The horizontal resolution is uniform, with 14 km separation between grid points. The vertical grid spacing is nonuniform. It is 12 km in the photosphere, chromosphere, and TR, and increases in the corona and convection zone, where the scale heights are larger.

The magnetic field configuration has two main opposite polarities of the size and strength (with 190 G unsigned mean magnetic field) of a medium-sized plage region (10 Mm) separated by 45 Mm. This leads to $\sim \! 50$ Mm long loops connecting the two polarities.

Concerning the boundary conditions, they are periodic in the horizontal direction and characteristic open boundaries in the vertical direction, allowing waves and plasma to go through without reflection; see the Appendix of Gudiksen et al. (2011) for further details about the characteristic boundary implementation. In addition, the bottom boundary has a constant entropy input in regions of inflow, to drive and maintain the solar convective motions, so the effective temperature at the photosphere of the simulations is \sim 5780 K. No new magnetic flux was added through the lower boundary.

Both simulations include ion—neutral interaction effects by adding two new terms in the induction equation: the Hall term and the ambipolar diffusion. The expanded induction equation is:

$$\frac{\partial \mathbf{B}}{\partial t} = \nabla \times \left[\mathbf{u} \times \mathbf{B} - \eta \mathbf{J} - \frac{\eta_{\mathrm{H}}}{|\mathbf{B}|} \mathbf{J} \times \mathbf{B} + \frac{\eta_{\mathrm{A}}}{\mathbf{B}^{2}} (\mathbf{J} \times \mathbf{B}) \times \mathbf{B} \right], \tag{1}$$

where B, J, u, η , $\eta_{\rm H}$, and $\eta_{\rm A}$ are the magnetic field, current density, velocity field and magnetic diffusivity, Hall term coefficient, and the ambipolar diffusion coefficient. The first term on the right-hand side of the induction equation is the convective term, and the second term represents the ohmic diffusion. The ohmic diffusion is not treated in the *Bifrost* code, since the hyperdiffusion terms typically are much larger than the ohmic diffusion (Martínez-Sykora et al. 2017a). The third term, the Hall term, does not lead to energy dissipation, but the ambipolar diffusion term (the last one) leads to additional heating owing to dissipation of currents that are perpendicular to the magnetic field:

$$Q_{\rm A} = \eta_{\rm A} J_{\perp}^2, \tag{2}$$

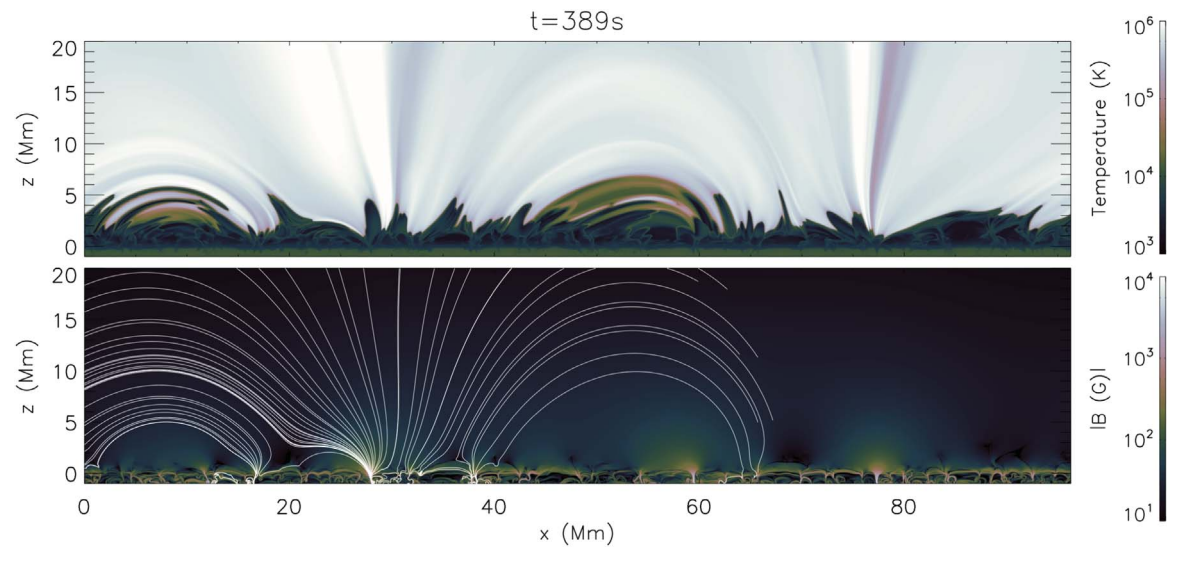


Figure 1. Temperature (top) and magnetic field strength (bottom) in the gol_nei simulation at t = 390 s after switching on the NEI. Magnetic field lines (bottom) are shown on the left-hand side only in order to clearly show the magnetic field structure on the right-hand side. Note that the numerical domain spans from 3 Mm below the surface (z = 0 Mm) to 40 Mm above the surface, so these maps only show the lower atmosphere. An animation showing the time evolution is available. The animation begins at t = 200 s and ends at t = 909 s. The realtime duration of the video is 7 s. (An animation of this figure is available.)

with Q_A being the ambipolar heating per unit volume and J_{\perp} the current density perpendicular to the magnetic field.

The Hall term depends on the electron number density, while the ambipolar diffusion depends on the ion–neutral collision frequency and ionization fraction:

$$\eta_{\rm H} = \frac{|\mathbf{B}|}{q_{\rm e} n_{\rm e}},\tag{3}$$

$$\eta_{\rm A} = \frac{(\rho_n/\rho)^2 |\mathbf{B}|^2}{\sum_a \sum_{a'} \rho_{a0} \frac{m_{a'\hat{I}}}{m_{a'\hat{I}} + m_{a0}} \nu_{a0a'\hat{I}}};\tag{4}$$

where for clarity and consistency, we used the same nomenclature as in Ballester et al. (2018), i.e., species and the ionization states are referred with the subindices a and I, respectively, i.e., I=0 denotes neutrals and $\hat{I}=I\geqslant 1$ ions. Here, ρ_{α},m_{α} , and $\nu_{\alpha\beta}$ for any $\alpha\in[a0,a\hat{I}]$ or $\beta\in[a'0,a'\hat{I}]$ are the mass density, atomic mass, and ion–neutral collision frequency between various species. We define ρ and ρ_n to represent the total mass density and total neutral mass density ($\rho_n=\Sigma_a~\rho_{a0}$). Finally, n_e , and q_e are the electron number density and the electron charge. Note that $n_{a'\hat{I}}\nu_{a'\hat{I}a0}=n_{a0}\nu_{a0a'\hat{I}}$, as required by momentum conservation. Equation (4) assumes that all ionized species moves together. The ion–neutral collision frequency is:

$$\nu_{a0a'\hat{I}} = n_{a\hat{I}} \,\, \sigma_{a0a'\hat{I}} \sqrt{\frac{8 \,\, k_{\rm B} \, T}{\pi \mu_{a0a'\hat{I}}}} \,, \tag{5}$$

where T is the temperature, $\sigma_{a0a'\hat{I}}$ is the cross section between an ionized species and neutral species, and $k_{\rm B}$ is the Boltzmann constant (Mitchner & Kruger 1973; Vranjes et al. 2008). The quantity $\mu_{a0a'\hat{I}}$ is the reduced mass $\mu_{a0a'\hat{I}} = m_{a0}m_{a\hat{I}}/(m_{a0}+m_{a\hat{I}})$. The ion–neutral cross sections used are described in Vranjes & Krstic (2013). For further details about the ambipolar diffusion implementation, see the papers by Martínez-Sykora et al. (2017a) and D. Nóbrega-Siverio et al. (2019, in preparation).

In order to have a rough understanding of how the ambipolar diffusion coefficient varies with ionization fraction, let us consider a gas consisting of only hydrogen. Assuming a cross section independent of the thermal properties of the plasma, the ambipolar diffusion has the following proportionality:

$$\eta_{\rm A} \sim \frac{|\boldsymbol{B}|^2}{n_{\rm H}^2 \sqrt{T}} \frac{1 - F_{\rm Hion}}{F_{\rm Hion}},$$
(6)

with $n_{\rm H} = n_{\rm H\,I} + n_{\rm H\,II}$. As long as $F_{\rm Hion} < 0.1$, as is the case in most of the chromosphere, then the dependence on the ionization degree is approximately given by

$$\eta_{\rm A} \propto \frac{1}{F_{\rm Hion}}.$$
(7)

This has been done assuming only hydrogen, but note that one can conclude the same for the total ionization fraction (F_{ion}) . Taking into account the assumptions to reach Equation (7), it allows us to roughly estimate and understand the dependence of the ambipolar diffusion on the ionization fraction.

Our first numerical simulation (gol_lte) includes the Hall term and the ambipolar diffusion in LTE. This simulation is the one called "GOL" in Martínez-Sykora et al. (2017a, 2017b). Our second numerical simulation (gol_nei) also includes the Hall term and ambipolar diffusion just as in gol_lte, but instead of assuming LTE for the ionization balance, it computes the ionization balance in nonequilibrium for hydrogen and helium. This is done through solving equations for charge and energy conservation together with advection and time-dependent rate equations for each level of a six-level hydrogen atom and a three-level helium atom, following Leenaarts et al. (2007a) and Golding et al. (2016). Ionization is still assumed to follow LTE for all other species. For the NEI case, the ionization rate

equations for hydrogen and helium are solved:

$$\frac{\partial n_{alE}}{\partial t} + \nabla \cdot (n_{alE} \boldsymbol{u}) = \sum_{\substack{l'E' \neq lE}}^{n_{al}} n_{al'E'} P_{al'E'lE} - n_{alE} \sum_{\substack{l'E' \neq lE}}^{n_{al}} P_{alEl'E'}, \tag{8}$$

where n_{al} is the number of levels and $P_{alEl'E'}$ the transition rate coefficient between levels IE and I'E'. These equations are solved using operator splitting where the continuity part (lefthand side of Equation (8)) is, like for the MHD equations, stepped forward in time using the modified explicit third-order predictor-corrector procedure (Hyman et al. 1979) allowing variations in time. After the predictor step, the rate part of the equations (right-hand side of Equation (8)) is calculated and the fundamental variables and hydrogen and helium populations are updated after a full time-step (Leenaarts et al. 2007a; Golding et al. 2016). As mentioned, the energy and charge are conserved and are detailed in Golding et al. (2016). H₂ molecules are also treated in nonequilibrium; for details, see Leenaarts et al. (2011). Note that only three-body reactions have been used. The NEI degrees and electron densities are used in the computation of η_H and η_A .

We refer to Martínez-Sykora et al. (2017a) for further details on the setup of the *gol_lte* simulation. In order to mitigate the numerical expenses of these simulations due to the NEI and/or GOL, we first ran the simulation without ambipolar diffusion and the Hall term for 35 minutes. Once transients from the initial conditions disappeared, we carried out the *gol_lte* simulation. Finally, when this simulation also reached a steady situation (after 15 minutes), we ran the *gol_nei* simulation. All simulations were run for another 12 minutes, at least, after transients from the initial setup for each case have disappeared, but we note that the simulations are not started from the same initial conditions—and thus only can be compared in a statistical sense. These transients disappear after a "first" shock or wave goes through the chromosphere; see, e.g., the movie in Leenaarts et al. (2007a).

3. Results

Martínez-Sykora et al. (2017a, 2017b, 2018), De Pontieu et al. (2017), and Khomenko et al. (2018) have, using radiative MHD numerical simulations, revealed the importance of ionneutral interaction effects in the solar chromosphere. Likewise, Carlsson & Stein (1992, 1994, 2002) and Carlsson et al. (1997) pointed out the importance of long timescales for NEI in the chromosphere. This was confirmed using 2D and 3D models by Leenaarts et al. (2007b, 2011) and Golding et al. (2016, 2017). Here, we will show that these effects must be considered together because the thermodynamics differ substantially between simulations that assume either LTE and/or a fully ionized atmosphere.

The differences between the *gol_lte* simulation and a case without ambipolar diffusion have already been described in detail in Martínez-Sykora et al. (2017a). We briefly summarize their main findings here: (1) numerical simulations without ambipolar diffusion do not generate type II spicules; and (2) cold bubbles that form behind the magneto-acoustic shocks due to the expansion (rarefaction) of the plasma are rather hot in the *gol_lte* simulation, because of heating through ambipolar diffusion.

NEI influences the effects of ambipolar diffusion, and the combination of these two processes (gol_nei) leads to different thermal structures than what is found when neither or only one of these processes is considered. Figure 2 zooms in on the chromosphere for each simulation: As in the gol lte simulation, in gol nei there are type II spicules (blue arrow in panel (G)) and low-lying loops (red arrow), but these spicules and loops have greater variations in temperature than those found in gol lte. Note that, within z = [1, 6] Mm, loops, shocks, and spicules have darker ($\sim 2 \times 10^3 \,\mathrm{K}$) and lighter colors $(\sim 4 \times 10^4 \text{ K})$ in panel (G) than in panel (B), where plasma is mostly accumulated around the temperature of ionization of hydrogen in LTE, i.e., $\sim 6 \times 10^3$ K (see also Section 3.3). The cold bubbles behind magneto-acoustic shocks (green arrows), mostly in the upper chromosphere, reach very low temperatures while magneto-acoustic shocks are hotter in the gol nei simulation (panel (G)). The thermal differences between gol lte and gol nei come from the ionization fraction (panels (C) and (H)) and the ambipolar diffusion (panels (D) and (I)). Any heating or cooling in NEI will increase or decrease the plasma temperature instead of ionizing or recombining hydrogen or helium in the medium. In addition, since the ionization degree is drastically different when assuming LTE (panel (C)) as compared to assuming NEI (panel (H)), the effects of ambipolar diffusion also differ (panels (D) and (I)). As a result, the location where ambipolar heating (panels (E) and (J)) occurs has changed, being large in some locations within type II spicules, low-lying loops, and in the shocks, but drastically reduced in cold bubbles and regions with strong expansion.

3.1. Statistical Properties

We now proceed with making a statistical analysis of the ionization fraction and ambipolar diffusion (Section 3.1.1), and of the thermodynamics within the chromosphere and TR (Section 3.1.2).

3.1.1. On the Ionization Fraction and Ambipolar Diffusion

When assuming LTE, both the ionization fraction ($F_{\rm ion}$) and ambipolar diffusion coefficient ($\eta_{\rm A}$) for a given magnetic field strength are uniquely defined by the temperature and density. This is because the ionization degree in LTE is set by Saha–Boltzmann statistics only. This is shown in panel (A) of Figure 3 for $F_{\rm ion}$, and in panel (E) for $\eta_{\rm A}$ for a magnetic field strength of 30 G. However, in NEI, $\eta_{\rm A}$, calculated from gol_nei , can vary by many orders of magnitude for a given temperature and density (panels (F)–(H), up to \sim 10 orders of magnitude), because in this case the ionization fraction also depends on the history of the plasma (panels (B)–(D)).

The ionization fraction and ambipolar diffusion have very different values when assuming LTE or NEI. In LTE (calculated from the LTE equation of state):

- 1. F_{ion} is small (highly neutral) below $\log T = [3.7 4]$ K, and large (highly ionized) above these temperatures (see panel (A) in Figure 3).
- 2. $\eta_{\rm A}$ becomes extremely large (up to $\sim 10^{16}~{\rm m}^2~{\rm s}^{-1}$) in the cold, low-density areas in the chromosphere, and negligible at high temperatures in upper chromosphere $(T>10^4~{\rm K})$ (see panel (E) in Figure 3 and Martínez-Sykora et al. 2017a).

In NEI (calculated from gol_nei):

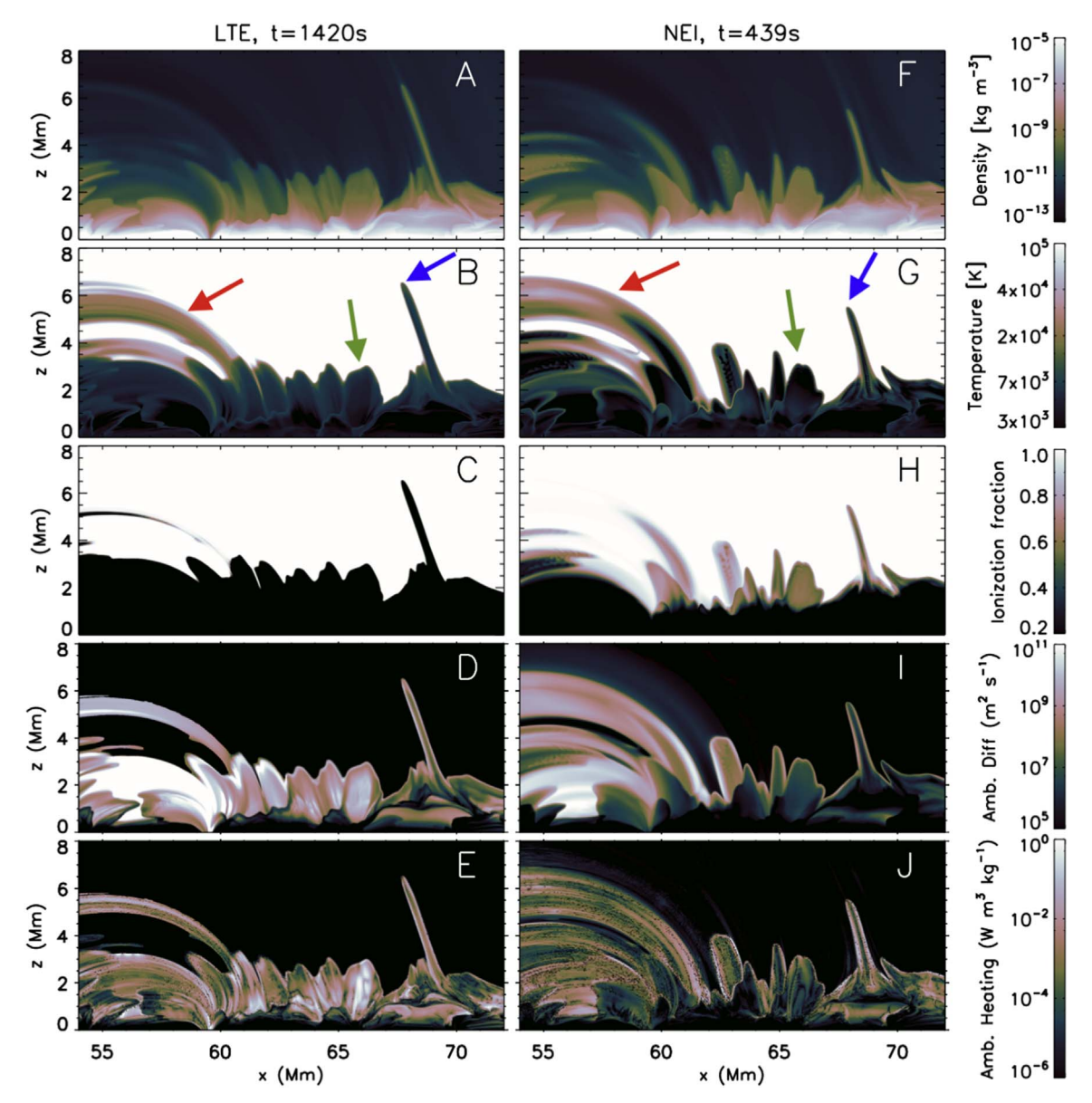


Figure 2. The thermodynamics in the chromosphere differs substantially between each model. Density (A, F), temperature (B, G), ionization fraction (C, H), ambipolar diffusion coefficient (D, I), and ambipolar heating (E, J) for the gol_lte (left), and gol_nei (right) simulations. The blue arrows point to a type II spicule in the simulations. The green arrows point to expanding bubbles of chromospheric gas following the passage of a shock wave, and the red arrows point to low-lying loops. An animation of the time evolution is available. The video begins at t = 970 s in the LTE model and t = 200 s in the NEI model. The video ends at t = 1650 s and t = 709 s, respectively. The realtime duration is 7 s.

(An animation of this figure is available.)

- 1. The median of the ionization fraction (panel (B)) is close to fully ionized, and the ambipolar diffusion coefficient (panel (F)) is at least five orders of magnitude smaller in regions with low densities ($\rho < 10^{-8} \, \mathrm{kg \ m}^{-3}$) and low temperatures ($T < 10^4 \, \mathrm{K}$) than what is obtained using LTE.
- 2. The ambipolar diffusion coefficient is much larger at high temperatures in the upper chromosphere $(T > 10^4 \text{ K})$ (panels (F) and (H)) as compared to the LTE case, because plasma, in NEI, is not fully ionized in these regions.

Consequently, we conclude that, in order to properly calculate ambipolar diffusion in the solar atmosphere, a proper treatment of the ionization fraction is required. As mentioned above, as a zero-order approximation, the ionization fraction and ambipolar diffusion coefficient are related by Equation (7). One can consider the validity of this relation by comparing the left and right column of Figure 3. However, this relation is imperfect because the ambipolar diffusion coefficient also depends on the number density and the temperature.

One method for estimating the importance of ambipolar diffusion is by dividing it with the Alfvén speed (u_a) : $L_{\rm amb} = \eta_{\rm A}/u_{\rm a}$. The quantity $L_{\rm amb}$ is the length scale on which ambipolar diffusion acts. Alfvén waves with wavelength similar to $L_{\rm amb}$, or currents perpendicular to the magnetic field (J_\perp) with characteristic spatial scales equal or smaller than $L_{\rm amb}$ will be efficiently diffused. Figure 4 shows the median and maximum values of $L_{\rm amb}$ in simulation gol_nei . Ambipolar diffusion can dissipate J_\perp on length scales as large as some tens of kilometers (up to a megameter) in extended regions in

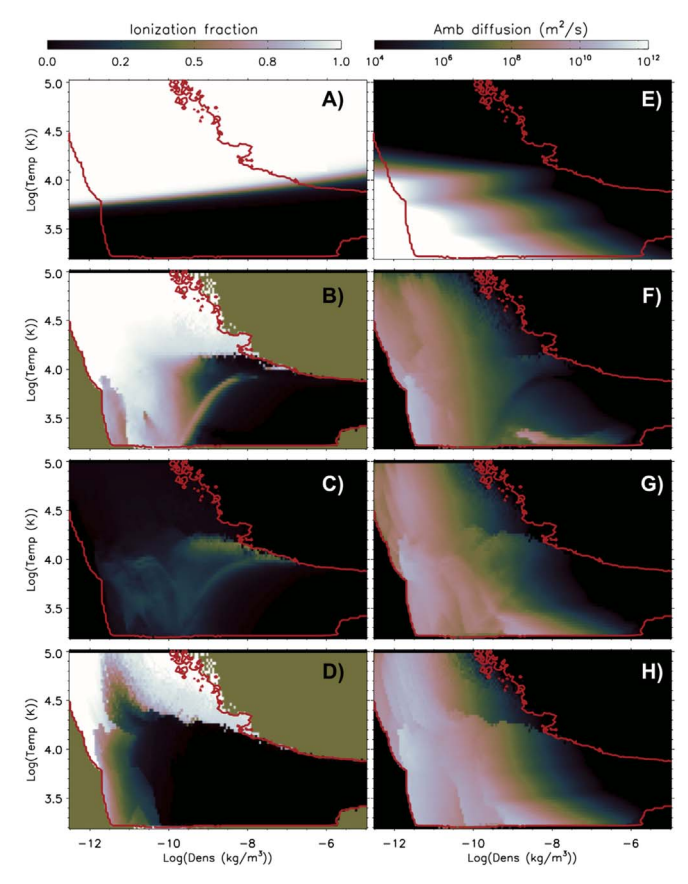


Figure 3. Distribution of the ionization fraction (left) and ambipolar diffusion coefficient (right) as a function of mass density and temperature, assuming a constant magnetic field strength of 30 G, computed from a 12 minute period of the simulation. Panels (A) and (E): assuming LTE. Panels (B)–(D) and (F)–(H): assuming NEI, as computed from simulation gol_nei . For this simulation, the ionization fraction and ambipolar diffusion are no longer uniquely determined by the temperature and mass density. We show the median of $F_{\rm ion}$ (B) and $\eta_{\rm A}$ (F), standard deviation of $F_{\rm ion}$ (C) and $\log \eta_{\rm A}$ (G), the minimum of $F_{\rm ion}$ (D), and the maximum of $\eta_{\rm A}$ (H). The red contours delineate the extrema in density and temperature for the gol_nei simulation. The data behind this figure are available in FITS format, except for the contours. The FITS file has the $191 \times 61 \times 8$ image in the primary extension, where the last dimension corresponds to each plot. The following three extensions provide the $10g_{10}$ mass density, $10g_{10}$ temperature, and the panel information, respectively.

(The data used to create this figure are available.)

chromospheric and TR plasma. The median of $L_{\rm amb}$ is above $10~{\rm km}~(10{\text -}10^3~{\rm km})$ for densities $10^{-9} < \rho < 10^{-7}~{\rm kg~m}^{-3}$ and low temperatures ($T \leqslant 3 \times 10^3~{\rm K}$) as well as at low densities ($\rho < 10^{-10}~{\rm kg~m}^{-3}$) and temperatures $T \leqslant 10^4~{\rm K}$. In addition, some plasma reaches large ambipolar diffusivities at densities $\rho < 4 \times 10^{-10}~{\rm kg~m}^{-3}$ and up to TR temperatures (see pink—white colors in the bottom panel of Figure 4). Note that the spatial grid spacing is $\sim \! 10~{\rm km}$ in this simulation, so anything smaller will not be resolved in the numerical simulation. Most of the currents in the simulation are highly confined, i.e., a few tens of kilometers (e.g., Hansteen et al. 2015; Nóbrega-Siverio et al. 2016; Martínez-Sykora et al. 2018).

3.1.2. On the Thermal Structure in the Chromosphere

Figure 5 shows Joint Probability Distribution Functions (JPDFs) of the density and temperature in each simulation, computed during a period of 12 minutes of solar time. Below,

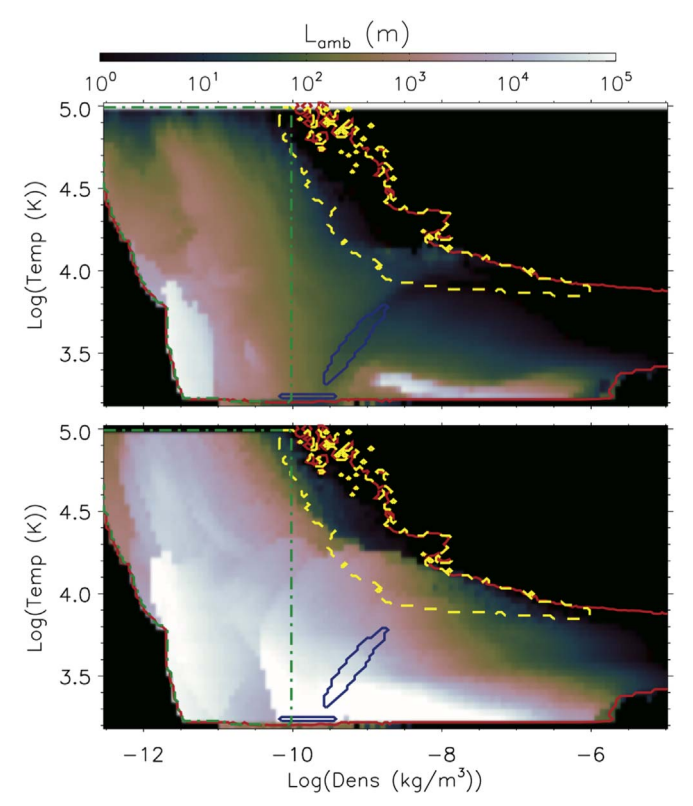


Figure 4. Ambipolar diffusion in gol_nei acts on currents perpendicular to the magnetic field with length scales of a few tens of kilometers. The distribution of the median (top) and maximum (bottom) of $L_{\rm amb}$ are shown for the gol_nei simulation as a function of temperature and density integrated over 12 minutes. Red contours delineate the temperature and density range of the entire simulated atmosphere. Solid blue, dashed yellow, and dashed–dotted green contours correspond to populations 1, 2, and 3 described in Figure 5 and Sections 3.3.1–3.3.3. The data behind this figure are available in FITS format, except for the contours. The FITS file has the $136 \times 46 \times 2$ image in the primary extension, where last dimension corresponds to each plot. The following three extensions provide the \log_{10} mass density, \log_{10} temperature, and the panel information, respectively.

(The data used to create this figure are available.)

we discuss the statistical differences in the thermal properties between the two simulations.

1. Simulation gol_lte (top panel of Figure 5) shows three horizontal pink-white stripes at $\log T = 10^{3.8}$, 10^4 , and 10^{4.3}. These temperatures mark the transition from H I to HII, He I to He II, and He II to He III with an LTE ionization balance. A large energy gain or loss is needed for gas to pass these temperatures, and gas temperatures consequently tend to cluster there. In the gol_nei simulation, these stripes are not present, owing to the slow ionization/recombination rates. This process is explained in detail in Leenaarts et al. (2011) and Golding et al. (2016). In gol_nei, the low-density upper chromosphere has a large range of temperatures. Note that, for instance, around $\rho \approx 10^{-10} \ {\rm kg \ m^{-3}}$, the pink-white patch extends over an order of magnitude in temperature, due to the presence of NEI, and this is where ambipolar diffusion can play a big role. The plasma in this temperature/density range corresponds mainly to the type II spicules and low-lying loops described in Sections 3.3.2–3.3.3.

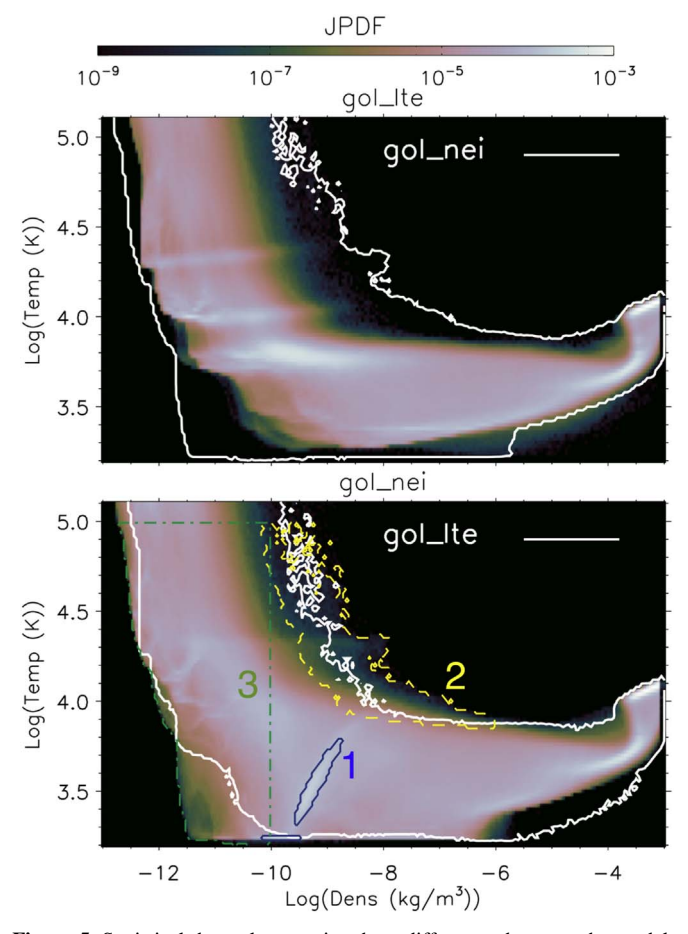


Figure 5. Statistical thermal properties show differences between the models, revealing the large impact of ion–neutral interaction effects and NEI. Joint Probability Distribution Function (JPDF) of temperature and density for gol_le (top panel) and gol_nei (bottom panel) simulations, each computed from a time series of 12 minutes of solar time. The white contours correspond to the temperature and density regime of the whole simulation at JPDF = 5×10^{-5} for the other simulation (see labels). Solid blue, yellow dashed, and green dashed–dotted contours are selected regions 1, 2, and 3, described in detail in Sections 3.3.1–3.3.3. The data behind this figure are available in FITS format, except for the contours. The FITS file has the $201 \times 150 \times 2$ image in the primary extension, where last dimension corresponds to each plot. The following three extensions provide the \log_{10} mass density, \log_{10} temperature, and the panel information, respectively.

(The data used to create this figure are available.)

2. Martínez-Sykora et al. (2017a) showed that the gas located in the wake of shocks (cold chromospheric bubbles) is efficiently heated in the *gol_lte* model. The larger temperatures in the wake of the shocks in the *gol_lte* simulation (top panel of Figure 5) result from heating through large ambipolar diffusion. The bubbles are cold and have low densities owing to the expansion. This plasma state leads to a large ambipolar diffusion (Equation (6)), and the ambipolar diffusion dissipates and/or advects almost all the currents that are perpendicular to the magnetic field out of the cold bubbles.

When hydrogen and helium are treated in NEI (gol_nei, bottom panel of Figure 5), extended regions of the cold chromospheric bubbles reach the minimum temperature set by the ad hoc heating term. Neither recombination nor the formation of H₂ molecules occurs fast enough to counter the cooling caused by adiabatic

expansion. Ambipolar diffusion is inefficient, in contrast to the gol_lte model: the ionization degree remains on the order of 10^{-2} in NEI, despite the low temperatures, and the ambipolar diffusion is therefore much weaker than in LTE, where the ionization degree can be as low as 10^{-10} . The gol_nei simulation does not reach even lower temperatures because of the ad hoc heating term in the model preventing temperatures from dropping below ~ 1800 K.

- 3. The gol_nei simulation has plasma with $-10 < \log \rho < -6$, with temperatures higher than reached in the gol_lte model. This is indicated with the yellow contour labeled 2 in the bottom panel of Figure 5. We analyze this population in Section 3.3.2.
- 4. The TR is less sharp in the gol_nei simulation than in the gol_lte . The JPDF shows slightly greater values within the TR in the gol_nei simulation (bottom panel). In addition, the density variation is largest in the gol_nei simulation at low TR temperatures $(4.0 \le log(T) \le 5.0)$. These thermal properties are due to the thermal evolution of type II spicules and low-lying loops resulting from NEI and ambipolar diffusion. See the detailed description of type II spicules and low-lying loops in Sections 3.3.2 and 3.3.3.
- 5. Finally, in gol_lte , a few dense ($\rho > 10^{-6}$ kg m⁻³) chromospheric plasma elements (JPDF $\approx 10^{-7}$) reach lower temperatures than in the gol_nei simulation. The dense chromosphere with low temperatures in the gol_lte simulation corresponds to a few regions that have accumulated enough magnetic flux in the photosphere to emerge. In such locations, the ambipolar diffusion allows the magnetic flux to expand, carrying dense plasma and producing rather large, cold bubbles (Martínez-Sykora et al. 2008; Tortosa-Andreu & Moreno-Insertis 2009; Ortiz et al. 2014). We do not see enough of such regions of accumulated magnetic flux at the photospheric heights in the gol nei simulation to produce similar events.

3.2. Impact of NEI on the Ambipolar Diffusion

The large disparity between the amplitude of ambipolar diffusion in LTE and that in NEI is mainly due to the ionization fraction (see Equation (4)), with a smaller contribution from temperature differences. The results of this section are related to the gol_nei simulation unless otherwise specified. Figure 6 and the associated animation show the fraction of H I, He I, and He II, as well as temperature, and the coefficient of the ambipolar diffusion. Panel (E) compares the electron number density assuming NEI ($n_{e_{\rm NEI}}$) with the electron number density computed in LTE ($n_{e_{\rm LTE}}$), following the expression:

$$r_{\rm ne} = \frac{n_{\rm e_{\rm NEI}} - n_{\rm e_{\rm LTE}}}{n_{\rm e_{\rm NEI}} + n_{\rm e_{\rm LTE}}}.$$
 (9)

Blue in panel (E) means that the electron number density—and therefore the ion number density—is smaller in NEI than in LTE, and red means the opposite. Under NEI conditions, the ionization fraction in the chromosphere departs from their corresponding ionization temperatures in LTE (the overlaying contours).

Figure 7 shows the important role of the ionization fraction under NEI conditions to the amplitude of ambipolar diffusion. Panel (A) of Figure 7 and the associated animation show the ambipolar diffusion coefficient of the *gol_nei* simulation. Panel

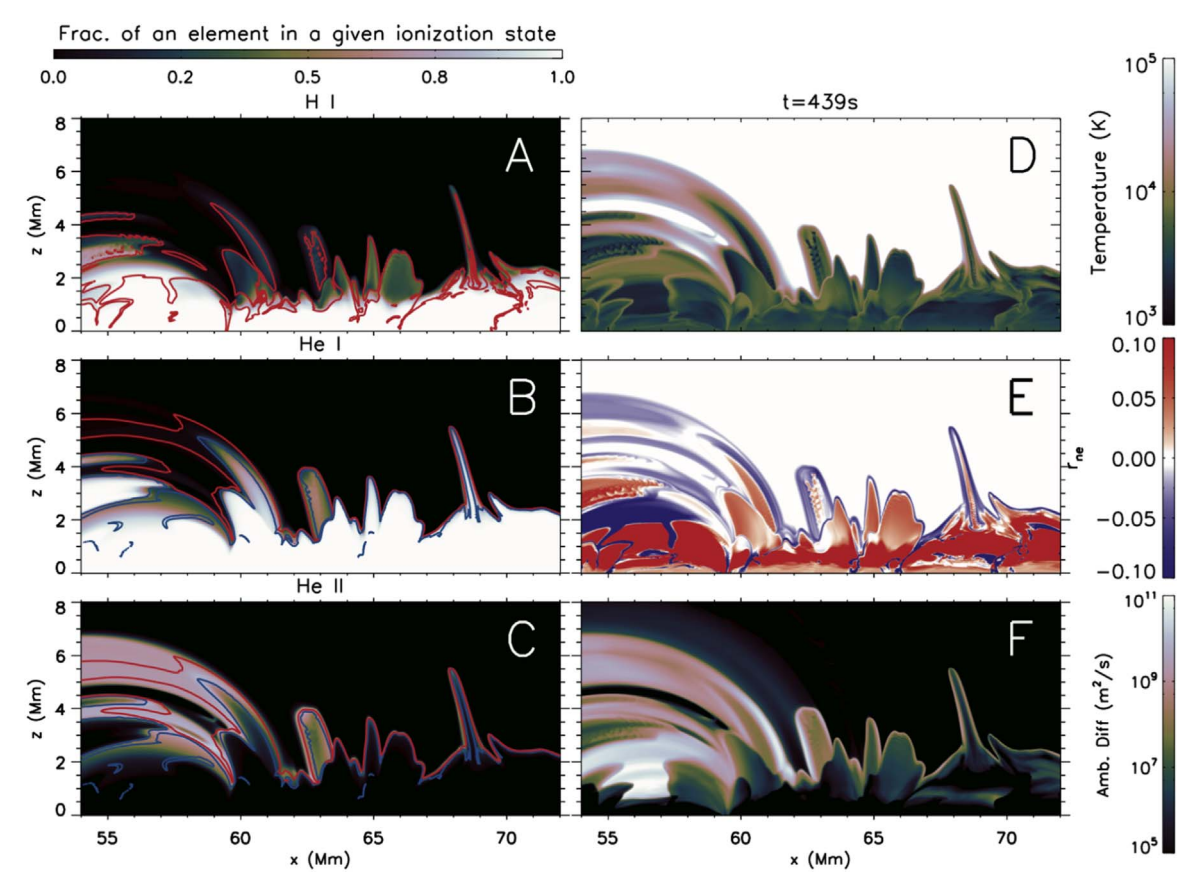


Figure 6. H and He are out of equilibrium in the chromosphere, which plays a role on the ambipolar diffusion coefficient. For this figure, we used only the gol_nei simulation. Panels (A)–(C): fraction of all atoms as H I, He I, and He II for the gol_nei simulation. The red contour in panel (A) shows where $T = 6 \times 10^3$ K, roughly where H I ionizes in LTE. The blue and red contours in panels (B) and (C) show $T = 10^4$ K and $T = 2.2 \times 10^4$ K, the temperatures where He I and He II start to ionize in LTE. Panel (D): temperature in gol_nei . Panel (E): the difference in electron density in NEI and LTE, as in Equation (9). This reveals regions where the ionization is out of equilibrium. Panel (F): the ambipolar diffusion coefficient in gol_nei . An animation showing the time evolution is available. The video starts at t = 200 s and ends at t = 909 s. The realtime duration of the video is 7 s. (An animation of this figure is available.)

(B) compares the ambipolar diffusion assuming NEI ionization ($\eta_{A_{\text{NEI}}}$) with the diffusion assuming LTE ionization ($\eta_{A_{\text{LTE}}}$) following the expression:

$$r_{\eta} = \frac{\eta_{\text{A}_{\text{NEI}}} - \eta_{\text{A}_{\text{LTE}}}}{\eta_{\text{A}_{\text{NEI}}} + \eta_{\text{A}_{\text{LTE}}}}.$$
 (10)

Red (blue) color means that ambipolar diffusion is underestimated (overestimated) under LTE conditions. Panel (C) shows the divergence of the velocity, showing the location of strong compression in shocks (blue) and regions that undergo expansion (red). Finally, panel (D) shows the current perpendicular to the simulated plane, which has been divided by the square root of the density in order to enhance the visibility of the currents at greater heights.

3.2.1. Cold Expanding Regions—Using the gol_nei Simulation

We find that most of the fluid is highly ionized in the cold plasma forming during the early phases of the rise of cold bubbles, as well as in thin cold regions within type II spicules and low-lying loops (green, blue, and red arrows in panels (B) and (G) in Figure 2).

In the low to middle chromosphere, the fraction of neutral hydrogen (H I, panel (A) in Figure 6) decreases at a height of $z \approx 1$ Mm, which also happens to always be at roughly at the

same density of 10^{-5} kg m⁻³ (see panel (F) in Figure 2). This is the location where the acoustic waves driven by convective motions at the photosphere become shocks due to the exponential density drop. Shocks appear (in blue in panel (C) of Figure 7) as a result of strong compression and behind the shock fronts, i.e., in the wake, cold bubbles form as the plasma expands (red). Shocks passing through the middle chromosphere ionize hydrogen (panel (A) in Figure 6). When nonequilibrium ionization is accounted for, shocks passing through the chromosphere ionize most of the hydrogen rapidly while the recombination timescales ($\sim 10^4$ s) are much longer than the hydrodynamic timescales (10-300 s). Consequently, the plasma stays ionized despite the drop in temperature in the cold bubbles (red in panel (E) in Figure 6). As a result of this, $\rho_{a\hat{l}} \nu_{a\hat{l}a'0}$ (see Equation (4)) is high and the coefficient of ambipolar diffusion is extremely low in NEI conditions (panel (I) in Figure 2). Therefore, the effects of ambipolar diffusion in LTE are highly overestimated in the cold bubbles (blue in panel (B) of Figure 7). It is only toward the end of the cold bubble evolution (a few minutes after the shock passes through) that the plasma starts to recombine and the effects of ambipolar diffusion increase in significance.

In NEI, regions with strong expansion in the upper chromosphere and TR appear as red in panel (C) of Figure 7. These regions are cold inside type II spicules and in low-lying loops, but are relatively ionized in hydrogen, while being

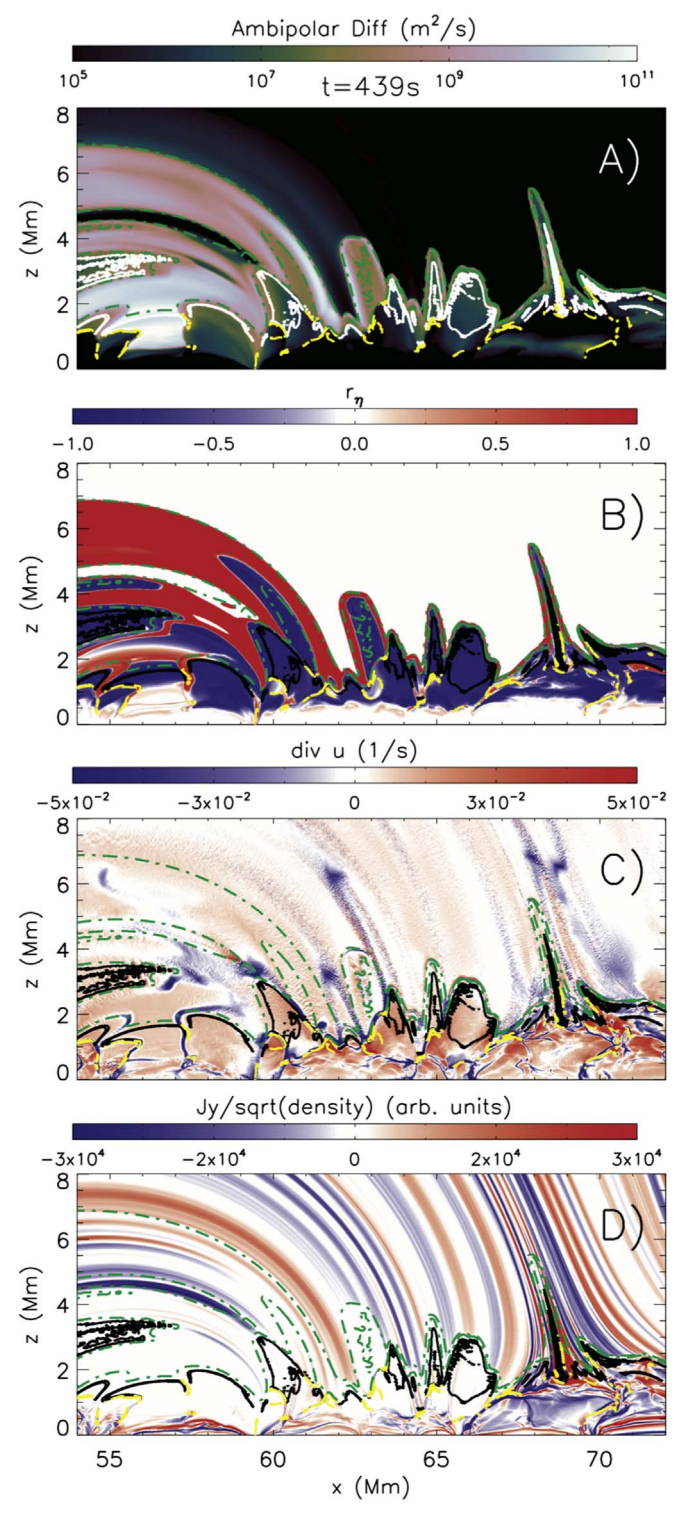


Figure 7. NEI has a great impact on the ambipolar diffusion. For this figure, we used only the *gol_nei* simulation. Panel (A): ambipolar diffusion coefficient. Panel (B): difference in ambipolar diffusion between NEI and LTE ionization (Equation (10)). Panel (C): divergence of the velocity. Panel (D): ratio of current perpendicular to the simulated plane and density. Grid points within the solid white (panel (A)) or black (panels (B)–(D)) correspond to points within the contour labeled 1 in the bottom panel of Figure 5. The yellow dashed contour corresponds to the points within the contour labeled 2, and the green dashed–dotted contour corresponds to the contour labeled 3 in Figure 5. An animation showing the time evolution is available. The video starts at t = 200 s and ends at t = 889 s. The realtime duration of the video is 7 s. (An animation of this figure is available.)

highly neutral in helium (panels (B) and (C) in Figure 6). As in the middle chromosphere, the long recombination timescales as compared to the timescales of plasma expansion lead to a large percentage of ionized hydrogen compared to what would be found in an atmosphere computed with the assumption of LTE (red in panel (E) in Figure 6). This leads to smaller effects of ambipolar diffusion in these strongly expanding regions than in the LTE case (blue regions in panel (B) of Figure 7).

These expanding regions (cold expanding bubbles and cold thin regions near the TR) are areas termed population 1 in the bottom panel of Figure 5, which will be described in further detail in Section 3.3.1. Statistically speaking, this shows that the medians of the coefficients of ambipolar diffusion $\eta_{\rm A}$ (panel (F) of Figure 3) and $L_{\rm amb}$ (top panel of Figure 4) are small for the plasma contained within the contour labeled 1 ($\eta_{\rm A} < 10^8\,{\rm m}^2~{\rm s}^{-1}$).

3.2.2. Shocks, TR, and Low-lying Loops—Using the gol_nei Simulation

The opposite process happens in magneto-acoustic shocks or in the steep temperature rise of the TR (green and yellow contours in Figure 7). The number of neutrals in these regions is larger than expected under the assumption of LTE (blue in panel (E) of Figure 6). This is true for both hydrogen (panel (A) of Figure 6) in chromospheric shocks and for helium (panel (B)) in the upper chromosphere and TR. In these locations, the time between shocks passing is long enough that a large amount of plasma has managed to recombine. In addition, ionization does not happen immediately, and furthermore, the timescales of ambipolar heating are slightly shorter than the ionization timescales. All of these effects added together leads to lower ionization fractions in these regions in NEI than in LTE (blue in panel (E) in Figure 6). Thus, these locations have a larger ambipolar diffusion in NEI than in LTE (red in panel (B) of Figure 7).

The regions with the largest effects of ambipolar diffusion are found in low-lying TR or chromospheric magnetic loops at times long after shocks have passed through (e.g., around $x \approx [54-60]$ Mm in Figures 6 and 7). In these loops, the density decreases due to the draining of plasma along the loops toward the photosphere. Magneto-acoustic shocks passing through these highly inclined loops are less frequent than in other, more vertical magnetic structures, because the change in effective gravity leads to a lower acoustic cutoff frequency (e.g., Heggland et al. 2007). Consequently, recombination timescales are short compared to the time that elapses between shocks propagating along these loops. In this case, neutrals become important, and due to the low density, the ion-neutral collision frequency is low, resulting in an extremely high ambipolar diffusion. Additionally, these loops have more neutrals, especially in helium (panel (B) in Figure 6) than they would have assuming LTE (blue in panel (E)). The overabundance of neutrals is probably not due to the timescales involved, but rather because under these conditions, the ionization state is better modeled by "coronal equilibrium" conditions, with collisional ionization being balanced by radiative recombination, which predicts more neutrals at a given temperature than what is found in LTE. This state of affairs is detailed for hydrogen in the top panels of Figure 4 of Rutten (2016). Helium behaves in the same manner. A consequence is that the heating timescales due to ambipolar diffusion are much shorter than the ionization timescales. The

ionization fraction, mostly in helium, in these regions can be severely overestimated when assuming LTE (see panels (B), (C), and (E) in Figure 6, and Section 3.3.3 for further details), and the ambipolar diffusion is larger in NEI than assuming LTE (red in panel (B) of Figure 7).

In short, the effects of ambipolar diffusion are affected by the choice of assumption for the ionization balance. Assuming one scenario or the other can provide opposite roles for the ambipolar diffusion: in those locations where ambipolar diffusion is large in LTE (cold bubble or inside expanding spicules), it seems unimportant under conditions of NEI; on the other hand, in those locations where the ambipolar diffusion is small in LTE (e.g., shock fronts), with NEI the ambipolar diffusion is large enough to play an important role (as detailed below).

3.3. Impact of NEI and Ambipolar Diffusion on the Thermal Evolution

The previous section showed how NEI impacts ambipolar diffusion in the solar atmosphere. Now, we detail how these changes in the ambipolar diffusion impact the thermodynamics of the plasma.

3.3.1. Adiabatic Expansion

Let us consider the physical processes that play a role in the cold regions that lie along type II spicules or in the cold bubbles formed by rarefaction behind magneto-acoustic shocks. These regions in the gol_nei simulation are visible within the black contours in panels (B)–(D) of Figure 7. In the LTE models described by Martínez-Sykora et al. (2017a), cold bubbles and spicules are heated via ambipolar heating, which is the largest contributor. In those models, the ambipolar diffusion increases drastically, reaching values that rapidly dissipate any current or Aflvénic wave passing through. The ambipolar diffusion becomes extremely large because the ion-neutral collision frequency and ionization degree diminish (panel (D) in Figure 2, and panel (E) in Figure 3) as plasma expansion causes the temperature and density to fall rapidly. Consequently, cold regions behind the shocks are vigorously heated by the ambipolar heating (panel (E) in Figure 2). However, this situation changes once NEI is taken into account (right column in Figure 2). At that point, we find the cold bubbles to be much cooler; see Leenaarts et al. (2011), but cf. our discussion for comparison with the literature. Similarly, elongated thin structures inside type II spicules can be much cooler in the gol_nei simulation than in gol_lte (compare panels (B) and (G)

Going back to the JPDF maps in Figure 5, we mentioned a very intriguing population in the gol_nei simulation indicated with a solid blue contour labeled 1 in the bottom panel. We added white or black contours in the maps in Figure 7 that correspond to the plasma within this population. There, one can see that this population corresponds to the cold expanding bubbles (see animated Figure 7) as well as regions with strong expansion inside type II spicules. The slope of the contour labeled 1 in the bottom panel of Figure 5 follows $\rho \propto T^{5/3}$. This corresponds to the adiabatic relation between density and temperature. Statistically speaking, in these regions, the plasma behaves adiabatically. This has two causes: (1) ambipolar diffusion is not large enough to dissipate any current in the NEI case as opposed to in LTE, so the entropy sources are minor

(see below); and (2) recombination timescales are larger than expansion timescales, at least for the early stages of the lifetime of the bubbles, so recombination does not significantly change the plasma state.

In fact, in these regions, the timescales of the energy losses due to expansion can be as low as $\frac{1}{\nabla \cdot u} \approx 10$ s, which is much smaller than recombination timescales ($\sim 10^4$ s). In other words, cooling from expanding regions in simulations assuming LTE has a "reservoir" energy in the recombination energy of the ionized species. In contrast, in the simulation with nonequilibrium ionization/recombination (gol_nei), the cooling due to expansion is not using the "reservoir" energy in recombining the ionized species, due to the rather large recombination timescales. Instead, the temperature drops as dictated by the adiabatic expansion.

As mentioned before, in LTE (simulation *gol_lte*), the ambipolar diffusion increases abruptly with expansion (panel (D) in Figure 2 and associated animation) because of a decrease in ion–neutral collision frequency and ionization fraction (panel (C)). There, the ambipolar diffusion dissipates, or advects, almost any current or Alfvénic wave traveling through the cold bubbles (panels (D)–(F)).

In contrast to this, when modeling NEI (simulation *gol_nei*), ambipolar diffusion is nonexistent in these regions (Section 3.2.1), and thus the ambipolar heating there is negligible (panel (J) in Figure 2). Figure 8 shows the histogram of the ambipolar diffusion (top) and of the ambipolar heating (bottom) for the *gol_nei* simulation within the three selected regions: 1 (associated with the *adiabatic* expanding plasma; solid line), 2 (associated with the shocks; dashed line) and 3 (associated with low-density plasma; dotted line) shown in the bottom panel of Figure 5. Figure 8 confirms that the ambipolar diffusion is small and the ambipolar heating is negligible in the expanding cold bubbles and cold regions within the spicules (solid lines).

In simulation *gol_nei*, the Joule heating in cold bubbles is basically negligible, not only due to the rather low ambipolar diffusion, but also because most of the current and shocks are ahead of the cold bubble (panels (C)–(D) of Figure 7). In spicules, the region that corresponds to the population 1 (white contours in panel (A) of Figure 7) is highly confined along the spicule. Similarly, in these thin regions, the Joule heating is lower than in other locations within the spicule, since fewer and smaller currents are present.

3.3.2. Hot Shocks and Spicule Strands in the NEI Case

The second population of interest in this work has the opposite behavior. This population is indicated with the dashed yellow contour labeled 2 in the bottom panel of Figure 5 for simulation *gol_nei*. The plasma comprising this population is localized mostly in the shock fronts or boundaries and/or footpoints of type II spicules (yellow contours in Figure 7 and corresponding animation).

As mentioned above, in magneto-acoustic shocks and at sharp transitions with enough ambipolar diffusion and large currents, the ambipolar diffusion allows the dissipation of magnetic energy into heat. Therefore, ambipolar heating in the *gol_nei* simulation contributes to heating these locations (panel (J) in Figure 2 and corresponding animation). In fact, the ambipolar heating (dashed line in bottom panel of Figure 8) is up to an order of magnitude larger than inside the expanding cold bubbles (solid). The heat in shocks and those locations in spicules with large ambipolar diffusion comes not only from

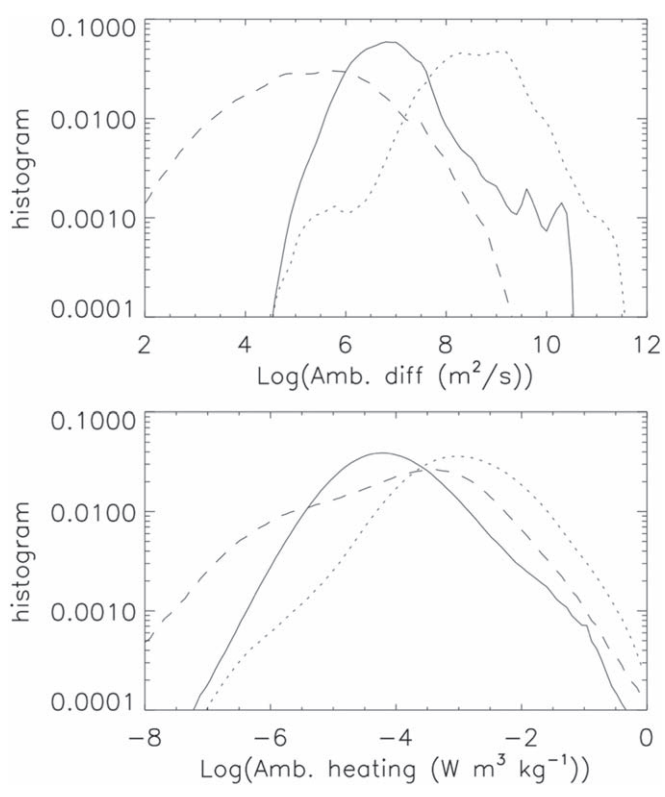


Figure 8. Histograms of the ambipolar diffusivity (top) and Joule heating through ambipolar diffusion (bottom) of the gol_nei simulation for the regions labeled 1 (associated with the *adiabatically* expanding plasma, solid line), 2 (associated with the shocks, dashed line) and 3 (associated with plasma with low density, dotted line) in Figure 5. Spicules have more Joule heating from ambipolar diffusion than in the expanding cold bubbles, and low-lying loops have the largest ambipolar diffusion. The data behind this figure are available in FITS. The FITS file has the 100×6 image in the primary extension where last dimension corresponds to each line plot. The following three extensions provide the log_{10} ambipolar diffusion axis, log_{10} ambipolar heating axis, and the line and panel information, respectively.

(The data used to create this figure are available.)

ambipolar heating, but also artificial diffusion, viscous heating, and compression. The timescales of all these heating processes can reach a similar order of magnitude (\sim 1 minute).

It is interesting to consider what this rapid heating in spicules means for a long-standing open question about the rapid apparent motions associated with spicules visible in TR lines. There are conflicting observations between type II spicules (typically observed spectrally with lines shifts showing line-ofsight velocities of up to $\sim 100 \, \mathrm{km \, s^{-1}}$), and apparent fast motions (the so-called network jets that show apparent speeds in the plane of the sky of a few hundred of km s⁻¹) (Beck et al. 2013; Tian et al. 2014; Rouppe van der Voort et al. 2015). De Pontieu et al. (2017) have shown that network "jets" do not necessarily involve very high plasma flows but can be caused by rapidly propagating heating fronts associated with ambipolar dissipation of currents traveling along type II spicules. The quoted work assumed LTE. In the current work, we relax the LTE assumption and investigate NEI conditions. The NEI calculations do not fundamentally change this picture. We again find that the extremely large currents in spicules (see bottom panel of Figure 7) are dissipated via ambipolar diffusion. The extremely large currents explain how this

population (dashed line versus solid line in Figure 8) can be subject to much larger ambipolar heating than what is found in cold expanding bubbles, despite the relatively smaller ambipolar diffusion in spicules. For instance, the example shown in panel (J) in Figure 2 reveals large heating occurring along the boundaries of (and inside of) the spicules. In other words, the NEI effects mostly affect the spatial distribution and (local) amount of heating, but do not not impact how fast a propagating current or Alfvén wave is propagating or dissipated. As in shock fronts, artificial diffusion, viscous heating, and compression also play an important role. In addition, spicules have temperature gradients high enough that thermal conduction contributes substantially to their thermal properties. The importance of each of these source terms varies within the spicules and evolution.

Due to the relatively large ionization timescales (a few tens of seconds) in these regions of the gol nei simulation, heating goes directly to increasing the plasma temperature instead of ionizing the plasma. Consequently, magneto-acoustic shocks are much hotter in the gol_nei simulation. In spicules, we find both: (1) cold regions with low ambipolar diffusion, low currents, large expansion, and large recombination timescales; and (2) hot regions with high ambipolar diffusion and large currents. These regions experience strong a temperature increase due to long ionization timescales. As a result of these two properties, spicules in *gol_nei* have large temperature variations within them. Note that, roughly when the spicule has fully formed, at its boundaries, the ambipolar diffusion can get as high as 10^{10} m² s⁻¹ (panel (A) in animated Figure 7). The large density and temperature variations within spicules may explain the apparently conflicting observations of temperatures and speeds in spicules (compare Beck et al. 2013; Tian et al. 2014; Rouppe van der Voort et al. 2015).

Another important aspect is that type II spicules seem to impact the associated coronal loops (Henriques et al. 2016; De Pontieu et al. 2017). Due to NEI effects, the amount of current (which, in our models, causes heating of coronal plasma) that pierces into the corona is larger than in the LTE case, and its role in the corona seems to be larger than what was previously reported by Martínez-Sykora et al. (2018). We find that the corona has on average 10% more current density in the *gol_nei* simulation than in the *gol_lte* simulation. A proper calculation of synthetic observables from this simulation and comparison with observations is required for further studies on the apparent motions and impact of spicules on the corona.

3.3.3. Low-density Low-lying Loops with Large Ambipolar Diffusion

As mentioned above, in NEI, low-lying loops with either chromospheric or TR temperatures show the largest ambipolar diffusion ($\eta_{\rm A} > 10^8~{\rm m}^2~{\rm s}^{-1}$, Section 3.2.2). These are regions of relatively low density ($10^{-12} < \rho < 10^{-9}~{\rm kg~m}^{-3}$), with temperatures $T < 10^5~{\rm K}$ (labeled as region 3 and shown with dashed–dotted green contours in Figures 5 and 7, and with dotted lines in Figure 8).

Since the ambipolar diffusion is larger in NEI than assuming LTE in low-lying loops (Section 3.2.2), the heating is also larger in NEI than in LTE. In NEI, heating from the ambipolar diffusion is more than an order of magnitude larger in these loops than in the other features described in the previous sections (dotted line in bottom panel of Figure 8). This is because the ambipolar diffusion coefficient is several orders of

magnitude larger in these loops (dotted line in top panel of Figure 8) than in the other features (dashed or solid lines). Consequently, almost any Alfvénic wave or current is dissipated there.

These low-lying loops share similarities with two different types of loops that are observed in the solar atmosphere: (1) loops that appear to outline the canopy and connect plage regions of opposite polarity in active regions, typically clearly visible in chromospheric (e.g., $H\alpha$) or TR (e.g., Si IV 1400 Å) diagnostics; (2) so-called Unresolved Fine Structure (UFS, Feldman 1983; Hansteen et al. 2014).

Our results suggest that "canopy loops" may be composed of plasma with a large range of temperatures due to NEI effects, "adiabatic" expansions, and ambipolar heating, with a mix of hot and cool strands right next to each other. In our simulations, these low-lying loops initially are filled with cool plasma due to shocks passing through from one footpoint all the way to the other footpoint (see animated Figures 2, 6, and 7). After the cold loop has formed, the fluid recombines, ambipolar diffusion increases, and the loop is heated up to TR temperatures via current dissipation from the ambipolar diffusion. This could explain the presence of chromospheric and TR loop-like structures that both appear to outline the canopy and occur in close proximity of one another.

Similarly, observations suggest that UFS loops seem to be formed by sporadic heating instead of cooling from hot loops (Hansteen et al. 2014; Brooks et al. 2016). Three-dimensional radiative MHD models (excluding ambipolar diffusion) show that the cycling of TR plasma starts with being first rapidly heated from chromospheric temperatures, to later drain and cool down in small magnetic loops (Guerreiro et al. 2013). Our model suggests that the ambipolar diffusion may play an important role in the thermal evolution of these low-lying loops: the ambipolar diffusion dissipates Alfvénic waves or currents into thermal energy. Since the ambipolar heating timescales are shorter or comparable to ionization timescales, most of the heating goes into heating the plasma instead of ionizing the plasma. In addition, the ambipolar diffusion is important all the way up to TR temperatures, even above helium ionization temperatures in LTE, owing to the large role of NEI as shown in Figures 2, 3, and 6.

4. Discussion and Conclusions

We have performed a 2.5D radiative-MHD simulation that self-consistently includes hydrogen and helium in nonequilibrium ionization and ion-neutral interaction effects (ambipolar diffusion and the Hall term). We have compared this model to a previously existing model that included only the ion-neutral interaction effects. Our results reveal that combining hydrogen and helium in NEI and ion-neutral interaction effects leads to substantial thermal differences compared to the model with LTE ionization. Ambipolar diffusion is influential in the solar chromosphere, but plays different and opposing roles depending on whether one assumes LTE or NEI when computing populations. In short, in NEI, the ambipolar diffusion and its Joule heating play a role in the thermodynamics in shock fronts, low-lying chromospheric and TR loops, and hot regions within type II spicules. In contrast, in LTE, the role of the ambipolar diffusion and associated Joule heating is negligible in shock fronts and important in post-shock plasma and cold regions within type II spicules.

The thermodynamic evolution of plasma in wakes produced by the rarefaction behind the magneto-acoustic shocks in the chromosphere resembles previous 2D radiative MHD models in revealing the large role of the NEI effects (Leenaarts et al. 2007a). During the first tens of seconds of the wake formation, the expansion is quasi-adiabatic where the entropy sources are minor. However, those previous simulations do not reveal the adiabatic expansion of population 1, most likely because plasma reached very rapidly the minimum temperature allowed by the imposed ad hoc heating (Leenaarts et al. 2007a, 2011). Most of the chromospheric plasma in their simulation was much cooler than in *gol_nei*, most likely due to a very weak magnetic field and lack of ambipolar diffusion in the former. At that temperature, an ad hoc heating term is added to avoid plasma temperatures outside the validity range of the equation of state.

Type II spicules have large temperature variations owing to nonequilibrium properties of hydrogen and helium and ionneutral interaction effects. Some plasma elements within the spicules become very cold due to a quasi-adiabatic expansion where the entropy sources are minor. Other plasma elements get heated due to strong currents traveling at Alfvén speed and dissipated via ambipolar and artificial diffusion (Tian et al. 2014; Narang et al. 2016; De Pontieu et al. 2017). In both scenarios, plasma is in NEI, and heating and cooling mostly change the temperature instead of ionizing or recombining the plasma. The heating associated with rapidly propagating currents and the complex temperature distribution within spicules may explain apparent discrepancies between various observations of temperature, velocities, and apparent speeds, e.g., by Rouppe van der Voort et al. (2015), Beck et al. (2013), and Tian et al. (2014).

Our gol_nei model suggests that low-lying loops outlining the canopy (e.g., in $H\alpha$ and TR lines) may be composed of multi-thermal threads that are formed by shocks passing through these loops. These shocks fill the loops with cold plasma, and due to the slow thermal evolution (compared to recombination timescales), ambipolar diffusion becomes important and heats the low-lying loops. Ambipolar diffusion becomes extremely large and leads to strong heating up to TR temperatures. Heating timescales are thus shorter than ionization timescales and the heating goes mostly toward increasing the temperature. We also speculate that heating in UFS loops may be caused by a similar mechanism.

In summary, heating from either the ambipolar or artificial diffusion, compression, or thermal conduction does not go directly toward ionizing the plasma, but instead it increases the temperature. Consequently, shocks, low-lying loops, and regions with large current in type II spicules are heated to greater temperatures than in the LTE models. Similarly, when quasi-adiabatic expansion takes place, the cooling does not use the reservoir energy from the recombination; instead, the plasma cools down. As a result of this, cold bubbles with inefficient entropy sources have an adiabatic relation between temperature and density, in contrast to what occurs in models based on LTE.

It is critical to properly treat the physical processes and the thermodynamics in the numerical models in order to correctly interpret the observations. Our results show that NEI and ambipolar diffusion play a significant role in the thermodynamics. These physical processes could potentially have a

large impact on opacities and chromospheric spectral profiles. Forward modeling of chromospheric lines from these models may thus shed light on the interpretation of complex chromospheric observations.

Our simulations are limited to 2.5 dimensions. In 3D, it is expected that shocks, cold bubbles, magnetic reconnection, and currents may change quantitatively, compared to a 2.5D scenario (e.g., Martínez-Sykora et al. 2019). In addition, in 3D, the convective motions build up more current in the atmosphere than in 2D. Despite these differences, we expect that our results are qualitatively robust thanks to the self-consistent implementation of the many processes included in our models.

We gratefully acknowledge support by NASA grants NNX16AG90G, NNX17AD33G, 80NSSC18K1285, and contract NNG09FA40C (IRIS), as well as NSF grant AST1714955. J.L. was supported by a grant (2016.0019) of the Knut and Alice Wallenberg foundation. The simulations have been run on clusters from the Notur project, and the Pleiades cluster through the computing project s1061, s1630, s1980, and s2053 from the High End Computing (HEC) division of NASA. This study has been discussed within the activities of team 399 "Studying magnetic-field-regulated heating in the solar chromosphere" at the International Space Science Institute (ISSI) in Switzerland. We have used IDL to analyze the data. This research is also supported by the Research Council of Norway through its Centres of Excellence scheme, project number 262622, and through grants of computing time from the Programme for Supercomputing.

ORCID iDs

Juan Martínez-Sykora https://orcid.org/0000-0002-

Jorrit Leenaarts https://orcid.org/0000-0003-4936-4211 Bart De Pontieu https://orcid.org/0000-0002-8370-952X Daniel Nóbrega-Siverio https://orcid.org/0000-0002-7788-6482

Viggo H. Hansteen https://orcid.org/0000-0003-0975-6659 Mats Carlsson https://orcid.org/0000-0001-9218-3139

References

```
Arber, T. D., Haynes, M., & Leake, J. E. 2007, ApJ, 666, 541
Ballester, J. L., Alexeev, I., Collados, M., et al. 2018, SSRv, 214, 58
Beck, C., Rezaei, R., & Puschmann, K. G. 2013, A&A, 556, A127
Braginskii, S. I. 1965, RvPP, 1, 205
Brooks, D. H., Reep, J. W., & Warren, H. P. 2016, ApJL, 826, L18
Carlsson, M., Judge, P. G., & Wilhelm, K. 1997, ApJL, 486, L63
Carlsson, M., & Leenaarts, J. 2012, A&A, 539, A39
Carlsson, M., & Stein, R. F. 1992, ApJL, 397, L59
Carlsson, M., & Stein, R. F. 1994, in Chromospheric Dynamics, ed.
   M. Carlsson (Oslo: Univ. Oslo), 47
Carlsson, M., & Stein, R. F. 2002, ApJ, 572, 626
Cowling, T. G. 1957, PhT, 10, 40
De Pontieu, B., De Moortel, I., Martinez-Sykora, J., & McIntosh, S. W. 2017,
     oJL, 845, L18
De Pontieu, B., Martens, P. C. H., & Hudson, H. S. 2001, ApJ, 558, 859
De Pontieu, B., Martínez-Sykora, J., & Chintzoglou, G. 2017, ApJL, 849, L7
```

```
Golding, T. P., Carlsson, M., & Leenaarts, J. 2014, ApJ, 784, 30
Golding, T. P., Leenaarts, J., & Carlsson, M. 2016, ApJ, 817, 125
Golding, T. P., Leenaarts, J., & Carlsson, M. 2017, A&A, 597, A102
Goodman, M. L. 2011, ApJ, 735, 45
Gudiksen, B. V., Carlsson, M., Hansteen, V. H., et al. 2011, A&A, 531, A154
Guerreiro, N., Hansteen, V., & De Pontieu, B. 2013, ApJ, 769, 47
Hansteen, V., De Pontieu, B., Carlsson, M., et al. 2014, Sci, 346, 1255757
Hansteen, V., Guerreiro, N., De Pontieu, B., & Carlsson, M. 2015, ApJ,
   811, 106
Hayek, W., Asplund, M., Carlsson, M., et al. 2010, A&A, 517, A49
Heggland, L., De Pontieu, B., & Hansteen, V. H. 2007, ApJ, 666, 1277
Henriques, V. M. J., Kuridze, D., Mathioudakis, M., & Keenan, F. P. 2016,
   ApJ, 820, 124
Hyman, J., Vichnevtsky, R., & Stepleman, R. 1979, Advances in Computer
   Methods for Partial Differential Equations - III (New Brunswick, NJ:
   International Association for Mathematics and Computers in
   Simulation), 313
Khomenko, E., & Collados, M. 2012, ApJ, 747, 87
Khomenko, E., Vitas, N., Collados, M., & de Vicente, A. 2018, A&A,
   618, A87
Leake, J. E., & Arber, T. D. 2006, A&A, 450, 805
Leake, J. E., & Linton, M. G. 2013, ApJ, 764, 54
Leenaarts, J., Carlsson, M., Hansteen, V., & Gudiksen, B. V. 2011, A&A,
   530, A124
Leenaarts, J., Carlsson, M., Hansteen, V., & Rutten, R. J. 2007a, A&A,
   473, 625
Leenaarts, J., Pereira, T. M. D., Carlsson, M., Uitenbroek, H., & De Pontieu, B.
   2013, ApJ, 772, 89
Leenaarts, J., Wedemeyer-Böhm, S., Carlsson, M., & Hansteen, V. H. 2007b,
   in ASP Conf. Ser. 368, The Physics of Chromospheric Plasmas, ed.
   P. Heinzel, I. Dorotovič, & R. J. Rutten (San Francisco, CA: ASP), 103
Martínez-Sykora, J., De Pontieu, B., Carlsson, M., et al. 2017a, ApJ, 847, 36
Martínez-Sykora, J., De Pontieu, B., Carlsson, M., & Hansteen, V. 2016, ApJL,
   831, L1
Martínez-Sykora, J., De Pontieu, B., De Moortel, I., Hansteen, V. H., &
   Carlsson, M. 2018, ApJ, 860, 116
Martínez-Sykora, J., De Pontieu, B., & Hansteen, V. 2012, ApJ, 753, 161
Martínez-Sykora, J., De Pontieu, B., Hansteen, V., & Carlsson, M. 2015,
   RSPTA, 373, 40268
Martínez-Sykora, J., De Pontieu, B., Hansteen, V. H., et al. 2017b, Sci,
   356, 1269
Martínez-Sykora, J., Hansteen, V., & Carlsson, M. 2008, ApJ, 679, 871
Martínez-Sykora, J., Hansteen, V. H., Gudiksen, B., et al. 2019, ApJ, 878, 40
Mitchner, M., & Kruger, C. H. 1973, Partial Ionized Gasses (New York:
Narang, N., Arbacher, R. T., Tian, H., et al. 2016, SoPh, 291, 1129
Nóbrega-Siverio, D., Moreno-Insertis, F., & Martínez-Sykora, J. 2016, ApJ,
   822, 18
Ortiz, A., Bellot Rubio, L. R., Hansteen, V. H., de la Cruz Rodríguez, J., &
   Rouppe van der Voort, L. 2014, ApJ, 781, 126
Parker, E. N. 2007, Conversations on Electric and Magnetic Fields in the
   Cosmos (Princeton, NJ: Princeton Univ. Press)
Rouppe van der Voort, L., De Pontieu, B., Pereira, T. M. D., Carlsson, M., &
   Hansteen, V. 2015, ApJL, 799, L3
Rutten, R. J. 2016, A&A, 590, A124
Skartlien, R. 2000, ApJ, 536, 465
Smith, R. K., & Hughes, J. P. 2010, ApJ, 718, 583
Soler, R., Ballester, J. L., & Zaqarashvili, T. V. 2015, A&A, 573, A79
Tian, H., DeLuca, E. E., Cranmer, S. R., et al. 2014, Sci, 346, A315
Tortosa-Andreu, A., & Moreno-Insertis, F. 2009, A&A, 507, 949
Vernazza, J. E., Avrett, E. H., & Loeser, R. 1981, ApJS, 45, 635
Vranjes, J., & Krstic, P. S. 2013, A&A, 554, A22
Vranjes, J., Poedts, S., Pandey, B. P., & de Pontieu, B. 2008, A&A, 478,
Wedemeyer-Böhm, S., & Carlsson, M. 2011, A&A, 528, A1
Zaqarashvili, T. V., Carbonell, M., Ballester, J. L., & Khodachenko, M. L.
   2012, A&A, 544, A143
```

Feldman, U. 1983, ApJ, 275, 367